Isotropic periodic sum of electrostatic interactions for polar systems

Xiongwu Wu^{a)} and Bernard R. Brooks Laboratory of Computational Biology, NHLBI, NIH, Bethesda, Maryland 20892, USA (Received 28 April 2009; accepted 9 June 2009; published online 8 July 2009)

Isotropic periodic sum (IPS) is a method to calculate long-range interactions based on homogeneity of simulation systems. Long-range interactions are represented by interactions with isotropic periodic images of a defined local region and can be reduced to short ranged IPS potentials. The original electrostatic three-dimensional (3D)-IPS potential was derived based on a nonpolar homogeneous approximation and its application is limited to nonpolar or weak polar systems. This work derived a polar electrostatic 3D-IPS potential based on polar interactions. For the convenience of application, polynomial functions with rationalized coefficients are proposed for electrostatic and Lennard-Jones 3D-IPS potentials. Model systems of various polarities and several commonly used solvent systems are simulated to evaluate the 3D-IPS potentials. It is demonstrated that for polar systems the polar electrostatic 3D-IPS potential has much improved accuracy as compared to the nonpolar 3D-IPS potential. For homogeneous systems, the polar electrostatic 3D-IPS potential with a local region radius or cutoff distance of as small as 10 Å can satisfactorily reproduce energetic, structural, and dynamic properties from the particle-meshed-Ewald method. For both homogeneous and heterogeneous systems, the 3D-IPS/discrete fast Fourier transform method using either the nonpolar or the polar electrostatic 3D-IPS potentials results in very similar simulation results. © 2009 American Institute of Physics. [DOI: 10.1063/1.3160730]

I. INTRODUCTION

Calculation of long-range interactions is the most expensive part in molecular simulations, while accuracy of longrange interactions is crucial for a successful simulation study. Many methods have been worked out to handle long-range interactions. One main category is the cutoff based methods. Energy switch, energy shift, force switch (FSW), and force shift, which have been widely used in simulation studies of protein and DNA systems, belong to this category. These methods are criticized for lack of physical basis² and for having the undesirable effects of abrupt truncations.^{2,3} Some methods with certain physical basis, such as the reaction field⁴ and the local molecular field,⁵ have been developed to treat electrostatic interactions and have been successfully applied in simulation studies.⁶ Wolf et al.⁷ proposed a "damped-shifted" potential to describe charge interactions in condensed phases by taking into account charge neutrality in the cutoff sphere and based on the observation that in condensed phases, electrostatic potential is short ranged. This method has been successfully applied in the study of ionic and liquid systems.⁸ Fennel and Gezelter⁹ further improved the method and found it remarkable to reproduce the energetic and dynamic results obtained with lattice summation techniques. Recently, a force-matching approach was proposed to map electrostatic interactions to short range empirical functions. ¹⁰ This approach does not need predefined functional form and can produce excellent empirical functions to describe effective interactions. The empirical manner of this approach limits it to interpolating applications. In other words, the mapped empirical potential function is good for the systems and conditions where its force matching is performed. Outside the force-matching systems and conditions, a careful validation is necessary.

The other category in the calculation of long-range interactions is the lattice sum based methods. ¹¹ These methods use images created by periodic boundary conditions (PBCs) to represent remote structures. Long-range interactions are calculated by summing over all the interactions with these images. Many methods have been developed to perform the calculation efficiently such as the particle-meshed-Ewald (PME) method. ¹² Methods of this category are widely believed to be accurate, even though some artificial effects may arise from the PBC symmetry. ¹³ However, the computation cost of these methods is normally about twice that of the cutoff methods, and their parallelization scale is not as good.

The isotropic periodic sum (IPS) method, 14,15 like the lattice sum method, is a summation based method. However, due to the continuous distribution of the so-called isotropic periodic images used for the summation, the sum of longrange interactions can be reduced to a pairwise function of particles within a local region. This reduced pairwise function, termed as the IPS potential, is short ranged and can be applied to simulations just as in the cutoff methods. Therefore, the IPS method has the lattice sum basis and can reach the cutoff efficiency. Further, the IPS method is not limited by energy types. The three-dimensional (3D)-IPS potentials of many energy types, such as electrostatic and Lennard-Jones energies, have been presented in our previous work.¹⁴ For homogeneous systems, the IPS method¹⁴ can be applied with a local region as small as a typical cutoff region, say, \sim 10 Å in radius. For heterogeneous systems, the 3D-IPS/

^{a)}Author to whom correspondence should be addressed. Tel.: 301-451-6251. FAX: 301-402-3404. Electronic mail: wuxw@nhlbi.nih.gov.

discrete fast Fourier transform (DFFT) method ¹⁵ provides an efficient way to allow a local region large enough to account for the heterogeneity for an accurate calculation of longrange interactions. Venable *et al.* ¹⁶ compared 3D-IPS/DFFT to PME and demonstrated that this method is highly accurate for simple bulk fluids, liquid/liquid and liquid/vapor interfaces, and lipid bilayers and monolayers. For lipid monolayers, 3D-IPS/DFFT is recommended over PME. ¹⁶

The IPS method is based on a homogeneous model filled with isotropic periodic images. The IPS potential is the result of summation over all these images. The accuracy of the IPS potential depends on how well the isotropic periodic model describes a real system. The original electrostatic 3D-IPS potential was derived based on a homogeneous system where particles are more or less the same, such as a monopole system. However, most molecular systems have opposite charges which form polar moments, and the oppositely charged particles are highly correlated with each other. These highly correlated opposite charges behave very differently from the particles in a monopole homogeneous system, which could cause significant errors in long-range interaction calculation in strong polar systems.

This work derives a polar electrostatic 3D-IPS potential based on opposite charge interactions. For easy of discussion, in this work we label the original electrostatic 3D-IPS potential as 3D-IPSn, and the polar electrostatic 3D-IPS potential as 3D-IPSp. Through several model systems of various polarities and several commonly used solvent systems, we demonstrate the improvement of 3D-IPSp over 3D-IPSn. In Sec. II, we describe the derivation of the 3D-IPS potentials and the algorithms to apply them to both homogeneous systems and heterogeneous systems. Comparisons with other methods are described in Sec. IV.

II. METHOD AND ALGORITHM

A. Nonpolar electrostatic 3D-IPS potential

Here we briefly describe the derivation of the nonpolar electrostatic 3D-IPS potential, 14 3D-IPSn. As shown in Fig. 1, a charge i has a local region around it. This local region is defined as a sphere with a radius R_c and centered on the charge. The images of the charge distribute on spherical shells centered at the charge and are called the isotropic periodic images. There are an infinite number of such shells around the charge to fill the space. From inside outward, the shells are labeled as $1, 2, \ldots, m, \ldots$ The mth shell has a radius of $2mR_c$.

For any charge j in the local region, it interacts with charge i and all the isotropic periodic images of charge i. Real charges outside the local region are not visible to charge i. Instead, outside the local region the space is filled with the images of the local region charges. The distribution of the isotropic periodic images is described by two type of images: shell images which distribute randomly on the shell and axial images which sit at the positions where the axis is linking the two charges crossing the shells.

The electrostatic interaction between the two charges q_i and q_j is

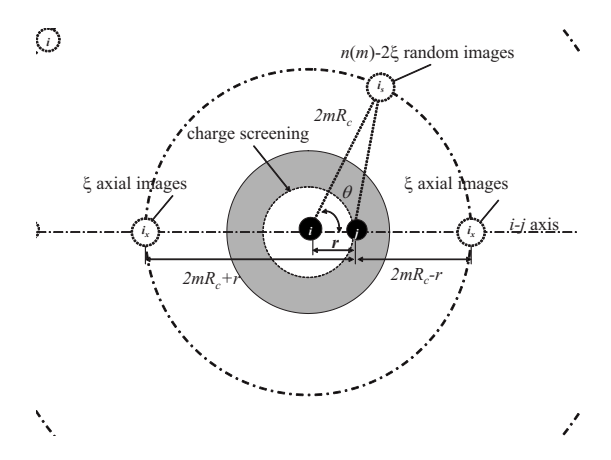


FIG. 1. The distribution of isotropic periodic images of particle i on its image shells. The mth image shell has a radius of $2mR_c$ and has $n(m) = 24m^2 + 2$ images. The images consist of 2ξ axial images and $n(m) - 2\xi$ random images. $\xi = 1$ is solved for electrostatic potential. For polar homogeneous systems the opposite charge screening effect creates a screening potential which depends on the distance from the center charge.

$$\varepsilon_{\text{ele}}(r) = \frac{q_i q_j}{r}.\tag{1}$$

The interaction of charge j with a shell image i_s on the mth shell can be calculated by the following integral:

$$\phi_{\text{shell}}(r,R_c,m) = \frac{1}{4\pi (2mR_c)^2}$$

$$\times \int_0^{2\pi} \int_0^{\pi} \varepsilon_{\text{ele}}(\sqrt{r^2 + (2mR_c)^2 - 4mR_c r \cos \theta})$$

$$\times (2mR_c)^2 \sin \theta d\theta d\varphi = \frac{q_i q_j}{2mR_c}.$$
 (2)

Here, r is the distance between charges i and j and θ is the angle between the line i-j and the line i- i_s . We drop subscript ij here for convenience.

The interaction between charge j and the axial images of charge i on the mth shell is

$$\phi_{\text{axial}}(r, R_c, m) = \varepsilon_{\text{ele}}(2mR_c - r) + \varepsilon_{\text{ele}}(2mR_c + r)$$

$$= \frac{q_i q_j}{2mR_c - r} + \frac{q_i q_j}{2mR_c + r}.$$
(3)

The number of images on each shell is proportional to the volume enclosing the shell,

$$n(m) = \frac{\frac{4}{3}\pi(2m+1)^3 R_c^3 - \frac{4}{3}\pi(2m-1)^3 R_c^3}{\frac{4}{3}\pi R_c^3}$$
$$= 24m^2 + 2. \tag{4}$$

If we assume that there are ξ axial images at each position where the i-j axis crosses a shell, there are $n(m)-2\xi$ random images on the mth shell. The total interaction of particle j with the images of particle i is

$$\phi_{\text{ele}}(r, R_c) = \sum_{m=1}^{\infty} ((n(m) - 2\xi)\phi_{\text{shell}}(r, R_c, m) + \xi\phi_{\text{axial}}(r, R_c, m)).$$
(5)

As explained in our previous work, ¹⁴ the isotropic periodic sum in the form of Eq. (5) does not converge for the electrostatic potential. Instead, Eq. (5) is calculated against a reference state where r=0. From Eq. (2) we can see that $\phi_{\text{shell}}(r,R_c,m)=q_iq_j/2mR_c$ is independent of r and is cancelled against the reference state. Therefore, the summation against the reference state depends only on the axial part

$$\begin{split} \phi_{\text{ele}}^{\text{3D-IPSn}}(r,R_c) &= \phi_{\text{ele}}(r,R_c) - \phi_{\text{ele}}(0,R_c) \\ &= -\xi \frac{q_i q_j}{2R_c} \left(2\gamma + \psi \left(1 - \frac{r}{2R_c} \right) \right. \\ &+ \psi \left(1 + \frac{r}{2R} \right) \right), \end{split} \tag{6}$$

where γ is the Euler constant, $\gamma = \lim_{m \to \infty} (\sum_{k=1}^{m} 1/k - \log m)$ $\approx 0.577\ 216$, and $\psi(z)$ is the digamma function: $\psi(z) = \Gamma'(z)/\Gamma(z)$ and $\Gamma(z) = \int_0^\infty t^{z-1} e^{-t} dt$.

Due to the periodicity along the distance, the forces from charge i and its images to charge j cancel when charge j is at the local region boundary of charge i,

$$\frac{\partial}{\partial r} (\varepsilon_{\text{ele}}(r) + \phi_{\text{ele}}^{\text{3D-IPSn}}(r, R_c)) \bigg|_{r=R_c} = 0.$$
 (7)

From Eq. (7) we can solve $\xi=1$. For an efficient calculation of 3D-IPSn in simulations, we used numerical functions obtained by fitting to the analytical solution, Eq. (6). ^{14,15} To avoid numerical mistakes and easy to program, we find that the following simplified polynomial with rationalized coefficients can well mimic Eq. (6),

$$\varepsilon_{\text{ele}}^{\text{3D-IPSn}}(r, R_c) = \varepsilon_{\text{ele}}(r) + \phi_{\text{ele}}^{\text{3D-IPSn}}(r, R_c)$$

$$\approx \frac{q_i q_j}{r} \left(1 + \frac{4}{13} \left(\frac{r}{R_c} \right)^3 + \frac{1}{26} \left(\frac{r}{R_c} \right)^5 + \frac{1}{26} \left(\frac{r}{R_c} \right)^7 \right). \tag{8}$$

Equation (8) has an average deviation of $7.7 \times 10^{-4} q_i q_j / R_c$ from Eq. (6).

B. Polar electrostatic 3D-IPS potential

For polar systems, the opposite charges play a screening effect to charge-charge interactions. As shown in Fig. 1, each charge is surrounded by an opposite charge distribution. Charge j interacts with both charge i and the opposite charge distribution of charge i. The opposite charge distribution plays a screening effect and the screening effect changes with the i-j distance. Such a screening effect can be described by a screening potential which changes with the displacement of the two charges. Due to the symmetry of the isotropic periodic images, it is reasonable to assume that the screening potential is an even function of the displacement between two particles,

$$\phi_{\text{screen}}(r, R_c) = s_1 \Delta^2 + s_2 \Delta^4 + s_3 \Delta^6 + \cdots$$

$$= s_1 r^2 + s_2 r^4 + s_3 r^6 + \cdots. \tag{9}$$

Here, Δ and r are the displacement and distance, respectively, and $r=|\Delta|$. The addition of the screening potential to the nonpolar 3D-IPS potential leads to the polar electrostatic 3D-IPS potential

$$\phi_{\text{ele}}^{\text{3D-IPSp}}(r, R_c) = \Phi_{\text{ele}}^{\text{3D-IPSn}}(r, R_c) + \phi_{\text{screen}}(r, R_c).$$
 (10)

First, let us consider the interaction between a charge q and a dipole μ_1 , assuming the dipole is at the same orientation as the distance vector. The dipoles can be represented as two charges separated by a distance d_1 , and its charges are $\pm \mu_1/d_1$. The charge-dipole interaction energy is

$$\begin{split} \varepsilon_{q\text{-dip}}^{\text{3D-IPSp}}(r,R_c) &= \lim_{d_1 \to 0} \frac{q\mu_1}{d_1} \bigg(\varepsilon_{\text{ele}}^{\text{3D-IPSp}} \bigg(r + \frac{d_1}{2},R_c \bigg) \\ &- \varepsilon_{\text{ele}}^{\text{3D-IPSp}} \bigg(r - \frac{d_1}{2},R_c \bigg) \bigg) \\ &= q\mu_1 \frac{\partial}{\partial r} \varepsilon_{\text{ele}}^{\text{3D-IPSp}}(r,R_c). \end{split} \tag{11}$$

Now let us consider two dipoles, μ_1 and μ_2 , both at the same orientation along the distance vector. The dipole-dipole energy is

$$\varepsilon_{\text{dip-dip}}^{\text{3D-IPSp}}(r,R_c) = \lim_{d_1 \to 0} \lim_{d_2 \to 0} \frac{\mu_1 \mu_2}{d_1 d_2} \left(\varepsilon_{\text{ele}}^{\text{3D-IPSp}} \left(r + \frac{d_1 - d_2}{2}, R_c \right) \right)$$

$$+ \varepsilon_{\text{ele}}^{\text{3D-IPSp}} \left(r + \frac{d_2 - d_1}{2}, R_c \right)$$

$$- \varepsilon_{\text{ele}}^{\text{3D-IPSp}} \left(r + \frac{d_1 + d_2}{2}, R_c \right)$$

$$- \varepsilon_{\text{ele}}^{\text{3D-IPSp}} \left(r - \frac{d_1 + d_2}{2}, R_c \right)$$

$$= - \mu_1 \mu_2 \frac{\partial^2}{\partial r^2} \varepsilon_{\text{ele}}^{\text{3D-IPSp}}(r, R_c). \tag{12}$$

Equations (11) and (12) can be also derived from Stone's electrostatic tensor formalism¹⁷ by modifying the electrostatic potential to the polar electrostatic 3D-IPS potential, $\varepsilon_{\rm ele}^{\rm 3D-IPSp}(r,R_c)$.

Due to the periodicity of the isotropic periodic images, the charge-dipole and dipole-dipole interactions have zero forces when the second object is at the local region boundary of the first object, i.e., when $r=R_c$,

$$\begin{split} f_{q\text{-dip}}^{\text{3D-IPSp}}(R_c, R_c) &= -q\mu_1 \left. \frac{\partial^2}{\partial r^2} (\varepsilon_{\text{ele}}(r) + \phi_{\text{ele}}^{\text{3D-IPSp}}(r, R_c)) \right|_{r=R_c} \\ &= 0, \end{split} \tag{13}$$

$$\begin{split} f_{\text{dip-dip}}^{\text{3D-IPSp}}(R_c, R_c) &= \mu_1 \mu_2 \left. \frac{\partial^3}{\partial r^3} (\varepsilon_{\text{ele}}(r) + \phi_{\text{ele}}^{\text{3D-IPSp}}(r, R_c)) \right|_{r=R_c} \\ &= 0. \end{split} \tag{14}$$

If we neglect r^8 and higher terms in Eq. (9) and substitute

Eq. (8) to Eq. (10), we can solve the parameters s_1, s_2, s_3 from boundary conditions, Eqs. (7), (13), and (14), and obtain the following expression for the polar 3D-IPS potential:

$$\varepsilon_{\text{ele}}^{\text{3D-IPSp}}(r, R_c) = \varepsilon_{\text{ele}}(r) + \phi_{\text{ele}}^{\text{3D-IPSp}}(r, R_c)$$

$$= \frac{q_i q_j}{r} \left(1 + \frac{35}{16} \left(\frac{r}{R_c} \right)^3 - \frac{21}{16} \left(\frac{r}{R_c} \right)^5 + \frac{5}{16} \left(\frac{r}{R_c} \right)^7 \right). \tag{15}$$

C. Lennard-Jones 3D-IPS potentials

Lennard-Jones potential does not have a polar effect and does not need polar modification. Lennard-Jones potential can be separated into repulsion and dispersion terms

$$\varepsilon_{\text{L-J}}(r) = \varepsilon_0 \left(\left(\frac{r^*}{r} \right)^{12} - 2 \left(\frac{r^*}{r} \right)^6 \right)$$

$$= \frac{A}{r^{12}} - \frac{C}{r^6}$$

$$= \varepsilon_{\text{ren}}(r) + \varepsilon_{\text{disp}}(r), \tag{16}$$

where ε_0 and r^* are the energy minimum and the minimum distance. $A = \varepsilon_0 r^{*12}$ and $C = 2\varepsilon_0 r^{*6}$ are the constants for repulsion and dispersion interactions, respectively. The 3D-IPS repulsion and dispersion potentials have been solved analytically. For efficient calculation in simulations, we used numerical functions to replace the analytical solutions. ^{14,15} We find that the following polynomials with rationalized coefficients can well mimic the analytic solutions,

$$\varepsilon_{\text{disp}}^{\text{3D-IPS}}(r, R_c) \approx -\frac{C}{r^6} \left(1 + \frac{7}{16} \left(\frac{r}{R_c} \right)^6 + \frac{9}{14} \left(\frac{r}{R_c} \right)^8 - \frac{3}{28} \left(\frac{r}{R_c} \right)^{10} + \frac{6}{7} \left(\frac{r}{R_c} \right)^{12} \right), \tag{17}$$

$$\varepsilon_{\text{rep}}^{\text{3D-IPS}}(r, R_c) \approx \frac{A}{r^{12}} \left(1 + \frac{5}{787} \left(\frac{r}{R_c} \right)^{12} + \frac{9}{26} \left(\frac{r}{R_c} \right)^{16} - \frac{3}{13} \left(\frac{r}{R_c} \right)^{20} + \frac{27}{26} \left(\frac{r}{R_c} \right)^{24} \right). \tag{18}$$

The average deviations of Eqs. (17) and (18) from the analytic solutions 14 are $6.2\times10^{-3}C/R_c^6$ and $3.7\times10^{-3}A/R_c^{12}$, respectively.

D. Application of 3D-IPS for homogeneous systems

For homogeneous molecular systems, a small local region defined by a typical cutoff distance is often enough to be a representative of remote structures. In this case, the local region radius is set to be the cutoff distance $R_c = r_c$, and 3D-IPS potentials are calculated directly for all atom pairs within the cutoff distance r_c . We call this implementation as the 3D-IPS method.

To avoid energy discontinuity crossing the boundary, a cutoff 3D-IPS potential is used for pairwise calculations,

$$\varepsilon^{C}(r, r_{c}) = \begin{cases} \varepsilon^{3\text{D-IPS}}(r, r_{c}) - \varepsilon^{3\text{D-IPS}}(r_{c}, r_{c}) & r \leq r_{c} \\ 0 & r > r_{c} \end{cases}, \quad (19)$$

where $\varepsilon^{\text{3D-IPS}}(r_c, r_c)$ is the 3D-IPS boundary energy. Here, we omit the energy-type subscript to indicate that the equation can be used for all energy types. The total cutoff energy is

$$E^{C}(r_c) = \frac{1}{2} \sum_{i}^{N} \sum_{j}^{N+M} \varepsilon_{ij}^{C}(r_{ij}, r_c).$$

$$(20)$$

Here, N is the number of particles in a system and M is the image particle generated from PBC. M=0 if there is no PBC. The double summation in Eq. (20) runs over all N particles for i and all N particles and all M image particles for j. Please note that the images generated from PBC are not the isotropic periodic images used to derive IPS potentials. The isotropic periodic images are purely imaginary and never explicitly exist or used in a simulation. Their contributions to long-range interactions are included in IPS potentials.

Based on homogenous approximation, the total boundary energy can be calculated by the following equation:

$$E^{B}(r_{c}) = \frac{1}{2} \sum_{i}^{N} \sum_{r_{ij} < r_{c}}^{N+M} \varepsilon_{ij}^{\text{3D-IPS}}(r_{c}, r_{c})$$

$$= \frac{2\pi r_{c}^{3}}{3V} \sum_{i}^{N} \sum_{j}^{N} \varepsilon_{ij}^{\text{3D-IPS}}(r_{c}, r_{c}). \tag{21}$$

Here, V is the volume of a PBC box. For a nonperiodic system, the middle expression must be used with M=0, while for a periodic system, the last expression can be used based on homogeneous approximation. The total energy is the cutoff energy plus the boundary energy

$$E^{\text{3D-IPS}}(r_c) = E^C(r_c) + E^B(r_c).$$
 (22)

E. Application of 3D-IPS for heterogeneous systems

For heterogeneous systems, the 3D-IPS/DFFT method 15 has been developed to tackle the heterogeneity of a system through a local region large enough to reach the homogeneity scale of a simulation system. The difference between 3D-IPS and 3D-IPS/DFFT methods is the size of the local region defined by R_c as compared to the cutoff region defined by r_c . The 3D-IPS method uses a local region identical to the cutoff region $R_c = r_c$ and directly calculates all pair interactions within the local region. The 3D-IPS/DFFT method uses a local region larger than the cutoff region $R_c > r_c$. A cutoff sum is calculated for particle pairs within r_c . The remaining interactions within R_c is calculated through the DFFT technique. For homogeneous systems where a small R_c comparable to the cutoff distance r_c can be used, the 3D-IPS method is an efficient way to calculate long-range interactions. While for heterogeneous systems where the homogeneity scale is large, it is highly inefficient to use the 3D-IPS method with a large cutoff distance. The 3D-IPS/DFFT

method separates the local region from the cutoff region so that a regular size cutoff region can be used to achieve efficient calculation.

The 3D-IPS/DFFT method is a two-step process. The first step calculates the cutoff sum by summing over particle pairs within a normal cutoff distance r_c , and the second step calculates the long-range correction which collects the remaining part using the DFFT technique. In our previous

study, ¹⁵ smoothing functions were used for the cutoff sum. In this work, we propose to directly use the 3D-IPS potentials, Eqs. (19) and (20), to calculate the cutoff sum, exactly the same way as described above for homogeneous systems by assuming $R_c = r_c$. Therefore, the cutoff sum represents the interaction as if the system is homogeneous. The long-range correction becomes a measurement of the deviation of the system from a homogeneous one,

$$\varepsilon^{LR}(r, r_c, R_c) = \varepsilon^C(r, R_c) - \varepsilon^C(r, r_c) = \begin{cases} \varepsilon^{IPS}(r, R_c) - \varepsilon^{IPS}(R_c, R_c) - \varepsilon^{IPS}(r, r_c) + \varepsilon^{IPS}(r_c, r_c) & r \le r_c \\ \varepsilon^{IPS}(r, R_c) - \varepsilon^{IPS}(R_c, R_c) & r_c < r \le R_c \\ 0 & r > R_c \end{cases}$$
(23)

The total long-range correction

$$E^{LR}(r_c, R_c) = \frac{1}{2} \sum_{i}^{N} \sum_{j}^{N+M} \varepsilon_{ij}^{LR}(r_{ij}, r_c, R_c)$$
 (24)

is calculated using the DFFT technique, which has been described in detail previously. ¹⁵ The total energy is the cutoff sum plus the long-range sum and plus the boundary energy

$$E^{\text{3D-IPS/DFFT}}(r_c, R_c) = E^C(r_c) + E^{\text{LR}}(r_c, R_c) + E^B(R_c). \tag{25}$$

F. Algorithm of the IPS method

To summarize the IPS method, we list the calculation equations for long-range interactions. This algorithm is for both homogeneous and heterogeneous systems as well as finite systems. Long-range interactions are assumed to be electrostatic and Lennard-Jones energies. Other energy types can be implemented in a similar way.

(1) Interactions within a cutoff distance r_c are calculated using Eq. (19). By substituting the IPS potentials, Eqs. (15), (17), and (18) to Eq. (19), we get the following equations:

$$\varepsilon_{\text{ele}}^{C}(r, r_c) = \begin{cases} \frac{q_i q_j}{r} \left(\chi_{\text{ele}} - \frac{35}{16} \left(\frac{r}{r_c} \right) + \frac{35}{16} \left(\frac{r}{r_c} \right)^3 - \frac{21}{16} \left(\frac{r}{r_c} \right)^5 + \frac{5}{16} \left(\frac{r}{r_c} \right)^7 \right) & r \le r_c \\ 0 & r > r_c \end{cases}$$
(26)

$$\varepsilon_{\text{disp}}^{C}(r, r_c) = \begin{cases} -\frac{C}{r^6} \left(\chi_{\text{L-J}} - \frac{67}{28} \left(\frac{r}{r_c} \right)^6 + \frac{9}{14} \left(\frac{r}{r_c} \right)^8 - \frac{3}{28} \left(\frac{r}{r_c} \right)^{10} + \frac{6}{7} \left(\frac{r}{r_c} \right)^{12} \right) & r \le r_c \\ 0 & r > r_c \end{cases} , \tag{27}$$

$$\varepsilon_{\text{rep}}^{C}(r, r_c) = \begin{cases} \frac{A}{r^{12}} \left(\chi_{\text{L-J}} - \frac{28}{13} \left(\frac{r}{r_c} \right)^{12} + \frac{9}{26} \left(\frac{r}{r_c} \right)^{16} - \frac{3}{13} \left(\frac{r}{r_c} \right)^{20} + \frac{27}{26} \left(\frac{r}{r_c} \right)^{24} \right) & r \le r_c \\ 0 & r > r_c \end{cases}$$

$$(28)$$

Here, χ_{ele} and $\chi_{\text{L-J}}$ are the electrostatic and Lennard-Jones scaling factors for covalent bonded atom pairs, respectively. Normally, they take the following form:

$$\chi = \begin{cases} 0, & 1-1, 1-2, \text{ and } 1-3 \text{ covalent bonded atom pairs,} \\ \chi^{(1-4)}, & 1-4 \text{ covalent bonded atom pairs,} \\ 1, & \text{otherwise.} \end{cases}$$

For the CHARMM27 force field, $\chi_{\text{ele}}^{(1-4)} = 1$ and $\chi_{\text{L-J}}^{(1-4)} = 1$. The cutoff sums are calculated over all pairs within r_c , as shown in Eq. (20), just like in other cutoff methods.

(2) For heterogeneous systems or finite systems, long-range corrections are calculated with Eq. (23). By substituting Eqs. (15), (17), and (18) to Eq. (23), we get the following equations:

$$\begin{aligned}
& = \begin{cases}
\frac{q_{i}q_{j}}{r} \left(-\frac{35}{16} \left(\frac{r_{c}}{R_{c}} - 1 \right) \left(\frac{r}{r_{c}} \right) + \frac{35}{16} \left(\left(\frac{r_{c}}{R_{c}} \right)^{3} - 1 \right) \left(\frac{r}{r_{c}} \right)^{3} - \frac{21}{16} \left(\left(\frac{r_{c}}{R_{c}} \right)^{5} - 1 \right) \left(\frac{r}{r_{c}} \right)^{5} + \frac{5}{16} \left(\left(\frac{r_{c}}{R_{c}} \right)^{7} - 1 \right) \left(\frac{r}{r_{c}} \right)^{7} \right) & r \leq r_{c} \\
& = \begin{cases}
\frac{q_{i}q_{j}}{r} \left(1 - \frac{35}{16} \left(\frac{r}{R_{c}} \right) + \frac{35}{16} \left(\frac{r}{R_{c}} \right)^{3} - \frac{21}{16} \left(\frac{r}{R_{c}} \right)^{5} + \frac{5}{16} \left(\frac{r}{R_{c}} \right)^{7} \right) & r_{c} < r \leq R_{c} \\
0 & r > R_{c}
\end{aligned}$$

$$\sum_{\substack{\text{elisp}\\\text{disp}}}^{\text{LR}}(r, r_c, R_c) \\
= \begin{cases}
-\frac{C}{r^6} \left(-\frac{67}{28} \left(\left(\frac{r_c}{R_c} \right)^6 - 1 \right) \left(\frac{r}{r_c} \right)^6 + \frac{9}{14} \left(\left(\frac{r_c}{R_c} \right)^8 - 1 \right) \left(\frac{r}{r_c} \right)^8 - \frac{3}{28} \left(\left(\frac{r_c}{R_c} \right)^{10} - 1 \right) \left(\frac{r}{r_c} \right)^{10} + \frac{6}{7} \left(\left(\frac{r_c}{R_c} \right)^{12} - 1 \right) \left(\frac{r}{r_c} \right)^{12} \right) & r \le r_c \\
-\frac{C}{r^6} \left(1 - \frac{67}{28} \left(\frac{r}{R_c} \right)^6 + \frac{9}{14} \left(\frac{r}{R_c} \right)^8 - \frac{3}{28} \left(\frac{r}{R_c} \right)^{10} + \frac{6}{7} \left(\frac{r}{R_c} \right)^{12} \right) & r_c < r \le R_c \\
0 & r > R_c
\end{cases}$$

$$(30)$$

$$\begin{split} \varepsilon_{\text{rep}}^{\text{LR}}(r,r_{c},R_{c}) \\ &= \begin{cases} \frac{A}{r^{12}} \left(-\frac{28}{13} \left(\left(\frac{r_{c}}{R_{c}} \right)^{12} - 1 \right) \left(\frac{r}{r_{c}} \right)^{12} + \frac{9}{26} \left(\left(\frac{r_{c}}{R_{c}} \right)^{16} - 1 \right) \left(\frac{r}{r_{c}} \right)^{16} - \frac{3}{13} \left(\left(\frac{r_{c}}{R_{c}} \right)^{20} - 1 \right) \left(\frac{r}{r_{c}} \right)^{20} + \frac{27}{26} \left(\left(\frac{r_{c}}{R_{c}} \right)^{24} - 1 \right) \left(\frac{r}{r_{c}} \right)^{24} \right) & r \leq r_{c} \\ \frac{A}{r^{12}} \left(1 - \frac{28}{13} \left(\frac{r}{R_{c}} \right)^{12} + \frac{9}{26} \left(\frac{r}{R_{c}} \right)^{16} - \frac{3}{13} \left(\frac{r}{R_{c}} \right)^{20} + \frac{27}{26} \left(\frac{r}{R_{c}} \right)^{24} \right) & r_{c} < r \leq R_{c} \\ 0 & r > R_{c} \end{cases} \end{split}$$

Normally, the repulsion potential does not need long-range correction. The total long-range corrections are calculated using Eq. (24) through the DFFT technique as described previously.¹⁵

(3) Boundary energies are precalculated based on Eq. (21). From Eqs. (15), (17), and (18), we have

$$E_{\text{ele}}^{B}(R_{c}) = \begin{cases} \frac{35}{32R_{c}} \left(\sum_{i}^{N} q_{i}\right)^{2} & \text{finite systems} \\ \frac{35\pi R_{c}^{2}}{24V} \left(\sum_{i}^{N} q_{i}\right)^{2} & \text{periodic systems,} \end{cases}$$
(32)

$$E_{\text{disp}}^{B}(R_{c}) = \begin{cases} -\frac{317}{224R_{c}^{6}} \sum_{i}^{N} \sum_{j}^{N} C_{ij} & \text{finite systems} \\ -\frac{317\pi}{168VR_{c}^{3}} \sum_{i}^{N} \sum_{j}^{N} C_{ij} & \text{periodic systems,} \end{cases}$$
(33)

$$E_{\text{rep}}^{B}(R_{c}) = \begin{cases} \frac{22101}{20462R_{c}^{12}} \sum_{i}^{N} \sum_{j}^{N} A_{ij} & \text{finite systems} \\ \frac{14734\pi}{10231VR_{c}^{9}} \sum_{i}^{N} \sum_{j}^{N} A_{ij} & \text{periodic systems.} \end{cases}$$
(34)

Obviously, for neutral systems, we have $E_{\text{ele}}^B(R_c)=0$. For repulsion interactions, we always use $R_c=r_c$, and no long-range correction is calculated.

(4) Using Eq. (25) to calculate total long-range interactions, the cutoff sum $E^{C}(r_c)$, the long-range correction $E^{LR}(r_c, R_c)$, and the boundary energies $E^{B}(R_c)$ are calculated by Eq. (20), Eq. (24), and Eqs. (32)–(34), respectively. For homogeneous systems, by setting $R_c = r_c$ we have $E^{LR}(r_c, r_c) = 0$ and only $E^{C}(r_c)$ and $E^{B}(r_c)$ need be calculated as shown by Eq. (22).

FIG. 2. Models with different polarities. These molecules are built based on hydrogen chloride by deleting or adding hydrogen atoms.

III. SIMULATION DETAILS

To examine the applicability of the 3D-IPSn and 3D-IPSp potentials, we designed four model systems of various polarities: monopole Cl-, dipole HCl, linear quadrupole H_2Cl , and multipole H_4Cl (Fig. 2). These four model systems were built from a hydrogen chloride molecule by deleting or adding hydrogen atoms. The charge on a hydrogen atom was 0.172 units and the charge on a chloride atom was set to neutralize the molecule except for the monopole system where the charge on a chloride atom was -0.172 units. The Lennard-Jones parameters were taken from the CHARMM force field: $\varepsilon_0^{\text{H}^+}$ =-0.046 kcal/mol, $r^{*\text{H}+}$ =0.449 Å, $\varepsilon_0^{\text{Cl}-}$ =-0.150 kcal/mol, and $r^{*\text{Cl}-}$ =4.54 Å. All H–Cl bonds have a length of 2.55 Å. The bond angle H–Cl–H in H₂Cl was 180° with a force constant of 500.0 kcal mol rad². In H₄Cl, the bond angles H-Cl-H between neighboring hydrogen atoms were 109.5° with a force constant of 100.0 kcal mol rad². In addition to these model systems, we also performed comparison simulations with water, ethanol, diethyl ether, and waterethanol mixture as well as a water interface system. Table I lists the systems simulated in this work.

For a systematic comparison, each system was simulated with a series of methods as listed in Table II. The FSW

TABLE I. Systems simulated in this work. The interfacial system has a box size of $40\times40\times80$ ų and the rest of the systems have a $40\times40\times40$ ų cubic PBC.

Systems	Molecules	Molecule number		
Monopole	Cl-	1331		
Dipole	HCl	1331		
Quadrupole	H ₂ Cl	1331		
Multipole	H ₄ Cl	1331		
Water	H_2O	2108		
Ethanol	C_2H_5OH	729		
Water-ethanol mixture	$H_2O+C_2H_5OH$	1000 H ₂ O+343 C ₂ H ₅ OH		
Diethyl ether	$C_2H_5OC_2H_5$	371		
Interfacial system	H_2O	2108		

method is compared for its wide use in biological computational studies. The FSW method uses the following electrostatic energy function:¹

$$\varepsilon_{\text{ele}}^{\text{FSW}}(r, r_{\text{on}}, r_c) = \begin{cases}
\frac{q_i q_j}{r} & r \leq r_{\text{on}} \\
\frac{q_i q_j}{r} \frac{(r_c^2 - r^2)^2 (r_c^2 + 2r^2 - 3r_{\text{on}}^2)}{(r_c^2 - r_{\text{on}}^2)^3} & r_{\text{on}} < r \leq r_c \\
0 & r > r_c
\end{cases} (35)$$

The switch-on distance was set to $r_{on}=r_c-2$ Å as recommended by the authors.

The force-damped-shifted method (FDS) proposed by Fennell and Gezelter⁹ is a very recent method that has been demonstrated to be excellent in reproducing PME results. Therefore, a comparison with FDS will be interesting. The electrostatic energy function of the FDS method takes the following form:

$$\varepsilon_{\text{ele}}^{\text{FDS}}(r, r_c) = \begin{cases} q_i q_j \left(\frac{\text{erfc}(\alpha r)}{r} - \frac{\text{erfc}(\alpha r_c)}{r_c} + (r - r_c) \left(\frac{\text{erfc}(\alpha r_c)}{r_c^2} + \frac{2\alpha \exp(-\alpha^2 r_c^2)}{\sqrt{\pi} r_c} \right) \right) & r \le r_c \\ 0 & r > r_c \end{cases}$$
(36)

A dumping factor of α =0.2 was used as recommended by the authors.

For the PME method, 12,19 the sixth order b-spline interpolation was used. The grid sizes were around 1 Å and the width of the Gaussian distribution κ was set to be 0.34. To focus the comparison on electrostatic interactions, Lennard-Jones interactions were calculated with either 3D-IPS or 3D-IPS/DFFT using Eqs. (27), (28), (30), (31), (33), and (34). The cutoff distance r_c , which for 3D-IPS is also the local region radius R_c , was set to 10 Å by default. For 3D-IPS/DFFT, the local region radius R_c was set to twice that of the longest side of the PBC box if not otherwise stated. The grid sizes were set to $r_c/4$, except otherwise stated. The order of b-spline was set to 6 for 3D-IPS/DFFT calculation. In Table

II, PME+3D-IPS represents a combination of PME for electrostatic interactions and 3D-IPS for Lennard-Jones interactions. Similarly, FSW+3D-IPS, FDS+3D-IPS, and PME+3D-IPS/DFFT are combinations of the corresponding methods.

The 3D-IPS and 3D-IPS/DFFT methods have been implemented into CHARMM (Ref. 20) and are available in CHARMM version c35. The CHARMM force field version 27 was used in all simulations reported here. All systems were simulated for 2 ns at a constant temperature of 300 K and a constant volume in a $40 \times 40 \times 40$ Å³ cubic periodic box, except the interfacial water system, which is in a $40 \times 40 \times 80$ Å³ orthorhombic periodic box. All simulations were performed on a quad-core 2.2 GHz Opteron computer. The

TABLE II. Nonbonded energy calculation methods used for comparison.

Methods	Electrostatic energy	Lennard-Jones energy	Notes	
FSW+3D-IPS	FSW ^a	3D-IPS	$r_c = R_c = 10 \text{ Å}, r_{on} = 8 \text{ Å}$	
FDS+3D-IPS	FDS^b	3D-IPS	$r_c = R_c = 10 \text{ Å}, \ \alpha = 0.2$	
PME+3D-IPS	PME^{c}	3D-IPS	$r_c = R_c = 10 \text{ Å}$	
PME+3D-IPS/DFFT	PME^{c}	3D-IPS/DFFT	$r_c = 10 \text{ Å}, R_c = 80 \text{ Å}$	
3D-IPSn	3D-IPSn	3D-IPS	$r_c = R_c = 10 \text{ Å}$	
3D-IPSp	3D-IPSp	3D-IPS	$r_c = R_c = 10 \text{ Å}$	
3D-IPSn/DFFT	3D-IPSn/DFFT	3D-IPS/DFFT	$r_c = 10 \text{ Å}, R_c = 80 \text{ Å}$	
3D-IPSp/DFFT	3D-IPSp/DFFT	3D-IPS/DFFT	$r_c = 10 \text{ Å}, R_c = 80 \text{ Å}$	

^aReference 1.

SHAKE algorithm²¹ was used to fix bond lengths and a time step of 2 fs was used.

IV. RESULTS AND DISCUSSION

The 3D-IPSn and 3D-IPSp potentials were derived based on different homogeneous systems and their accuracy in describing long-range interactions depends on system polarity. To examine the polarity dependence, we designed the four model systems of various polarities as listed in Table I. Comparison simulations were also performed with several commonly used solvent systems to demonstrate the improvement of 3D-IPSp over 3D-IPSn. To cover thermodynamic, structural, and dynamic properties, we compare energies, radial distribution functions (RDFs), and diffusion coefficients of these systems. The PME results are used as standards for the comparison. Through a water interface system, we demonstrate the application of these potentials to heterogeneous systems.

A. Energies

Table III compares the average potential energies from simulations with different energy calculation methods. For the monopole (Cl-) system, potential energies are not comparable because PME assumes a neutralized system while the other methods depend on the number of atom pairs within the cutoff distance or the local region radius. For the dipole system, HCl, 3D-IPSn and 3D-IPSp energies have similar differences from the PME+3D IPS results. For the quadru-

pole $\rm H_2Cl$ and multipole $\rm H_4Cl$ systems as well as all the solvent systems, it is apparent that 3D-IPSp energies are much closer to the PME+3D-IPS energies than 3D-IPSn energies. Clearly, the FSW and FDS energies have significant differences up to 2000 kcal/mol for water from the PME+3D-IPS energies. For all systems except the monopole system, the 3D-IPSn/DFFT energies are very close to the 3D-IPSp/DFFT energies, and both are very close to the PME+3D-IPS/DFFT energies.

Overall, these results indicate that for homogeneous systems, 3D-IPSp is better than 3D-IPSn to reproduce PME energies with a local region radius of about 10 Å. With the 3D-IPS/DFFT method, where the local region radius is large, both 3D-IPSn and 3D-IPSp potentials are effective in reproducing PME energies. FSW and FDS are not accurate in electrostatic energy description.

B. Radial distribution functions

RDFs are sensitive to potential functions and often show abnormal deviations for cutoff based methods around the cutoff region. Figures 3(a)–3(d) compare the RDFs of the four model systems obtained in simulations with PME +3D-IPS, FSW, FDS, 3D-IPSn, and 3D-IPSp methods. The FSW results deviate significantly from the PME results for all model systems, and the deviation increases with system polarities. For the multipole system [Fig. 3(d)], the FSW RDF is significantly different from the PME result around

TABLE III. Average potential energies (kcal/mol) from simulations with different methods.

Systems	FSW	FDS	3D-IPSn	3D-IPSp	PME+3D IPS	3D-IPSn/ DFFT	3D-IPSp/ DFFT	PME+3D IPS/ DFFT
Cl-	19 399.6 ± 0.9	9415.5 ± 1.0	$13\ 936.1 \pm 0.9$	4697.9 ± 0.9	-3083.1 ± 0.9	$1.192\ 23 \times 10^6 \pm 1.0$	$602\ 725.3 \pm 1.0$	-3073.0 ± 1.1
HCl	-32.1 ± 0.7	-204.7 ± 0.6	-79.1 ± 0.6	-96.0 ± 0.7	-89.1 ± 0.7	-78.9 ± 0.7	-78.5 ± 0.7	-77.5 ± 0.8
H2C1	1596.3 ± 0.9	1109.6 ± 1.0	1430.8 ± 0.9	1391.5 ± 0.9	1395.0 ± 0.9	1405.3 ± 1.1	1407.2 ± 0.9	1405.8 ± 0.9
H4Cl	2186.6 ± 0.8	863.4 ± 1.1	1880.2 ± 0.9	1743.1 ± 1.0	1744.9 ± 1.0	1758.4 ± 1.0	1759.1 ± 1.2	1759.7 ± 1.4
Water	$-21\ 540.1 \pm 1.1$	-22704.3 ± 0.8	-20719.1 ± 1.0	-20586.0 ± 0.8	-20596.2 ± 0.8	-20582.2 ± 0.8	-20580.8 ± 0.8	-20592.8 ± 0.9
Ethanol	-6615.6 ± 1.5	-8444.6 ± 1.6	-7830.9 ± 1.6	-7794.3 ± 1.8	-7796.2 ± 1.3	-7786.7 ± 1.4	-7782.7 ± 1.6	-7788.2 ± 1.9
Water- ethanol mixture	$-13\ 031.7 \pm 1.8$	-14559.7 ± 1.6	-13 324.4 ± 1.4	-13 281.4 ± 1.4	$-13\ 276.8 \pm 1.6$	$-13\ 260.7 \pm 1.3$	$-13\ 259.3 \pm 1.4$	$-13\ 268.8 \pm 1.6$
Diethyl ether	-1063.2 ± 0.9	-1967.7 ± 0.9	-1756.0 ± 0.8	-1747.9 ± 0.9	-1737.6 ± 0.9	-1729.4 ± 0.8	-1729.6 ± 0.8	-1731.5 ± 0.9

^bReference 9.

^cReference 23.

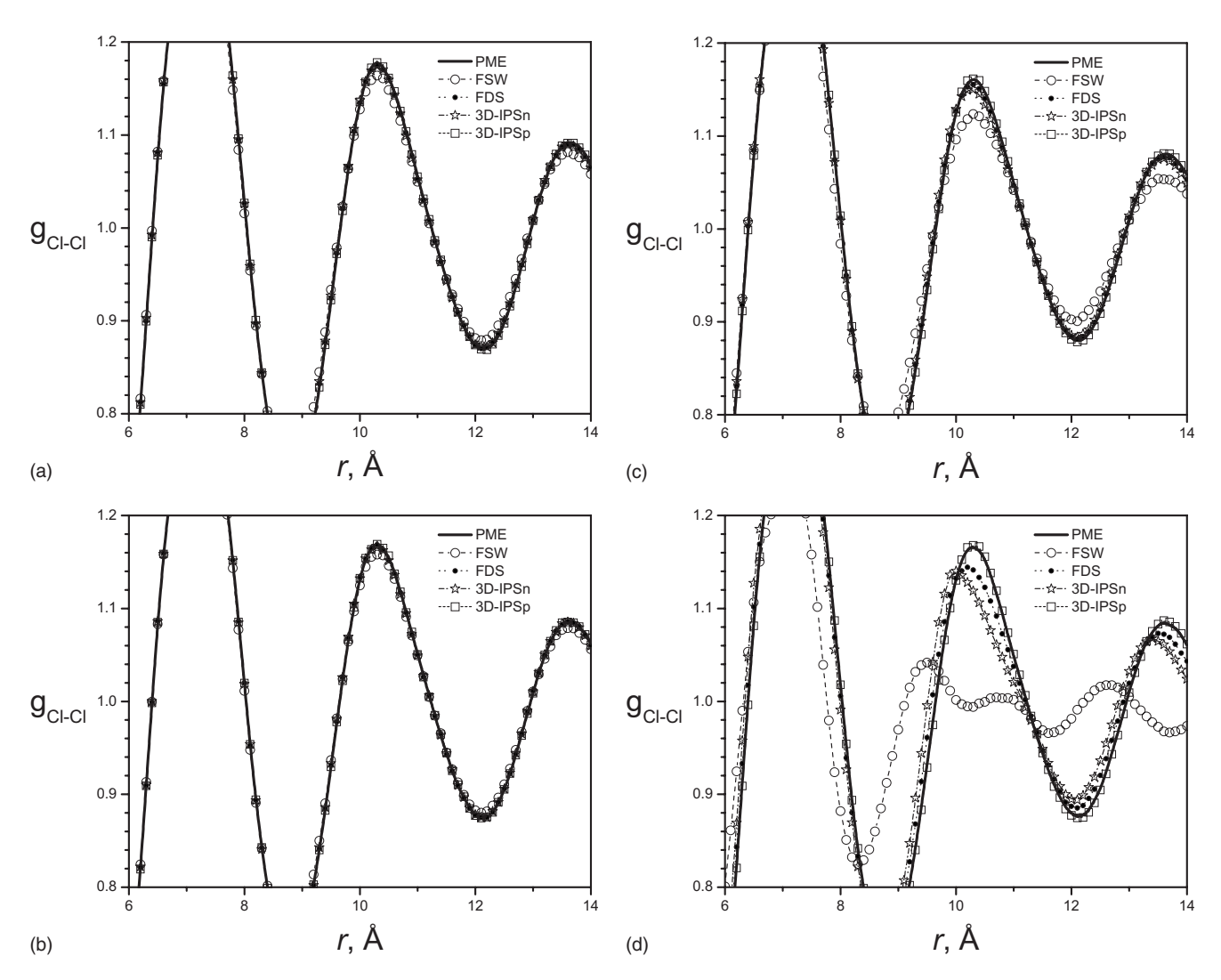


FIG. 3. Cl-Cl RDFs of the model systems. (a) Monopole, Cl-; (b) dipole, HCl; (c) linear quadrupole, H2Cl; (d) multipole, H4Cl.

the cutoff distance, 10 Å. The 3D-IPSn RDFs show a little deviation from the PME results for the monopole and dipole systems [Figs. 3(a) and 3(b)], but the deviations become apparent for the quadrupole and multipole systems [Figs. 3(c) and 3(d)]. Similarly, FDS results agree with the PME results for the monopole and dipole systems, while for quadrupole and multipole systems, FDS results show significant deviations from the PME results. The FDS deviations are smaller than the 3D-IPSn deviations. By contrast, 3D-IPSp produces RDFs almost identical to the PME results for all the model systems. The results of 3D-IPSn/DFFT and 3D-IPSp/DFFT are not shown in these figures because they almost completely overlap with the PME results.

To quantitatively measure the deviations, we calculated the root-mean-square deviations (RMSDs) of the RDFs (Table IV). The RMSDs of FSW, FDS, 3D-IPSn, and 3D-IPSp are calculated against the PME+3D-IPS results. The RMSDs of the 3D-IPSn/DFFT and 3D-IPSp/DFFT, as well as PME+3D-IPS, are calculated against the PME+3D-IPS/DFFT results. Normally, a RMSD less than 0.01 indicates a good agreement. For all the four model systems, the RMSDs of 3D-IPSp RDFs are between 0.001 and 0.002. For 3D-IPSn, the RMSDs are between 0.002 and 0.003 for the monopole and dipole systems but are as large as 0.029

for the multipole system. The RMSDs of FSW are significantly larger, while the RMSDs of FDS are smaller than that of 3D-IPSn but larger than that of 3D-IPSp. For both 3D-IPSn/DFFT and 3D-IPSp/DFFT, the RMSDs are all 0.002 or smaller. The RMSDs between the PME+3D-IPS results and the PME+3D-IPS/DFFT results are all 0.002 or smaller, indicating that for Lennard-Jones interaction, 3D-IPS with a local region radius of 10 Å produces very similar results as the 3D-IPS/DFFT results.

Figures 4(a)–4(d) further compare the RDFs in the four solvent systems. Again, FSW produces large deviations from the PME results. The 3D-IPSn and FDS methods also produce large deviations in RDFs, even though the deviations from FDS are smaller. By contrast, the 3D-IPSp RDFs show a dramatically improved agreement with the PME results. The RDFs of 3D-IPSn/DFFT and 3D-IPSp/DFFT are not shown here inasmuch as they are very close to each other and overlap almost completely with the PME results.

The RDF RMSDs for these solvent systems are also listed in Table IV. These RMSD data further support the observations from Figs. 3 and 4. Clearly, 3D-IPSp, as well as 3D-IPSn/DFFT and 3D-IPSp/DFFT, shows a dramatic improvement over FSW, FDS, and 3D-IPSn.

TABLE IV. RMSD of RDFs from various methods (FSW, FDS, 3D-IPSn, and 3D-IPSp are compared against PME+3D-IPS; PME+3D-IPS, 3D-IPSn/DFFT, and 3D-IPSp/DFFT are compared against PME+3D-IPS/DFFT).

Methods	FSW	FDS	3D-IPSn	3D-IPSp	PME+3D-IPS	3D-IPSn/DFFT	3D-IPSp/DFFT
Cl ⁻ :Cl-Cl	0.011	0.003	0.003	0.002	0.002	0.001	0.001
HCl:Cl-Cl	0.007	0.001	0.002	0.001	0.001	0.001	0.001
HCl:Cl-H	0.005	0.001	0.002	0.001	0.001	0.001	0.001
HCl:H-H	0.005	0.002	0.002	0.002	0.002	0.002	0.001
H ₂ Cl:Cl-Cl	0.027	0.004	0.007	0.002	0.001	0.001	0.001
H ₂ Cl:Cl-H	0.007	0.001	0.002	0.001	0.001	0.001	0.001
H ₂ Cl:H-H	0.003	0.001	0.001	0.001	0.001	0.001	0.001
H ₄ Cl:Cl-Cl	0.125	0.014	0.029	0.002	0.002	0.002	0.002
H ₄ Cl:Cl-H	0.027	0.003	0.007	0.001	0.001	0.001	0.001
H ₄ Cl:H-H	0.010	0.001	0.003	0.001	0.001	0.001	0.001
Water:O-O	0.047	0.009	0.015	0.001	0.002	0.001	0.001
Water:O-H	0.017	0.005	0.006	0.001	0.001	0.001	0.001
Water:H-H	0.009	0.003	0.003	0.001	0.001	0.001	0.001
Ethanol:O-O	0.046	0.010	0.009	0.003	0.004	0.003	0.002
Ethanol:O-H	0.030	0.010	0.012	0.004	0.002	0.003	0.003
Ethanol:H-H	0.037	0.007	0.012	0.004	0.004	0.004	0.003
Ether:O-O	0.081	0.014	0.028	0.006	0.004	0.004	0.004
Ether:O-H	0.028	0.005	0.010	0.003	0.002	0.002	0.002
Ether:H-H	0.012	0.002	0.005	0.001	0.002	0.003	0.001
Mixture: $O_w - O_w$	0.048	0.009	0.017	0.006	0.003	0.004	0.003
Mixture: $O_w - O_e$	0.040	0.008	0.014	0.003	0.002	0.005	0.002
$\underbrace{\text{Mixture:O}_e \text{O}_e}$	0.041	0.010	0.015	0.008	0.009	0.007	0.006

C. Diffusion coefficients

Diffusion coefficients measure the dynamic behavior of a simulation system. For molecular dynamics studies, it is desired that long-range interactions can be calculated in a way that dynamic properties can be preserved. We calculated the diffusion coefficients according to the mean square displacements of heavy atoms in these model systems and the solvent systems. Figure 5 shows the diffusion coefficients in the model systems as compared to the PME results. The lower panel is plotted against the PME+3D-IPS results and the upper panel is plotted against the PME+3D-IPS/DFFT results. Clearly, the FSW results deviate significantly from the PME results. The 3D-IPSn and the FDS results agree with the PME results for the monopole and dipole systems while having apparent deviations for the quadrupole and multipole systems. Obviously, the deviation increases as the polarity increases, indicating 3D-IPSn as well as FDS, and is limited to nonpolar or weak polar systems. For all the four model systems, the 3D-IPSp results agree well with the PME results. Comparing the 3D-IPSn/DFFT and 3D-IPSp/DFFT results with the PME+3D-IPS/DFFT results (Fig. 5 top panel), it can be seen that all the three methods agree very

Figure 6 compares the diffusion coefficients of the four solvent systems. The lower panel shows the comparison with the PME+3D-IPS results and the upper panel shows the comparison with the PME+3D-IPS/DFFT results. Again, the FSW results have significant deviations except for ethanol. 3D-IPSn, FDS, and 3D-IPSp all produce similar results as PME except for water where the 3D-IPSn result shows a large deviation. These results further demonstrate that the 3D-IPSn potential is limited to weak polar systems, while the

3D-IPSp potential can be applied to all systems. From the top panel of Fig. 6 we can see that both 3D-IPSn/DFFT and 3D-IPSp/DFFT produce very similar results as PME +3D-IPS/DFFT, demonstrating again that for the 3D-IPS/DFFT method, both 3D-IPSn and 3D-IPSp potentials can be used.

D. Effect of the local region radius

The accuracy of an IPS potential depends on how well the IPS images represent remote structures. When a local region is larger than the homogeneous scale, it is representative, in terms of particle composition and conformation, of any remote region beyond the local region, and the interactions with remote regions can be similar to the interactions with images of the local region at corresponding places. A larger local region will be more representative of remote structures. For the 3D-IPS method, the local region size is defined by the local region radius or the cutoff distance. It would be interesting to examine how the local region radius affects the simulation results.

Table V lists the average energies, diffusion coefficients, and RDF RMSDs of the model systems and the solvent systems with the local region radius ranging from 6 to 12 Å, as well as the 3D-IPSp/DFFT results, which correspond to a local region radius of 80 Å (twice that of the box side), and the PME results. Clearly, at R_c =6 Å, which is rarely used as a cutoff distance for molecular systems, the simulation properties have significant deviation from 3D-IPSp/DFFT or PME results. However, at R_c =8 Å, the 3D-IPSp results are already very close to the 3D-IPSp/DFFT results or the PME

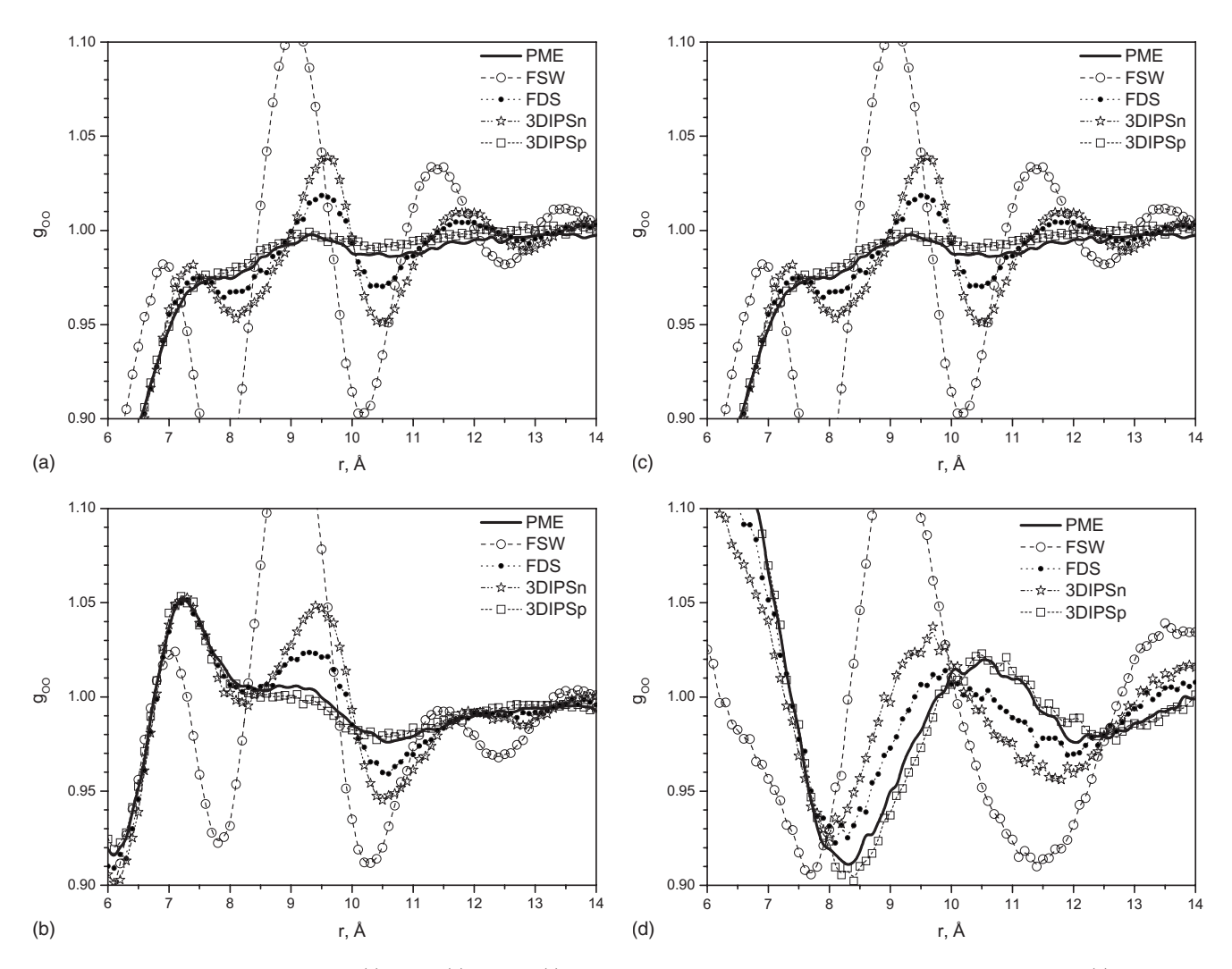


FIG. 4. O-O RDFs of the solvent systems. (a) Water; (b) ethanol; (c) water-ethanol mixture between water oxygen and ethanol oxygen; (d) diethyl ether.

results except for the monopole system. When R_c increases to 10, 12, and 80 Å, the agreements with the PME results are about the same.

The fact that, when $R_c > 8$ Å, the simulation results have little dependence on the local region radius, validates the assumption that the local region is representative of the remote regions in the simulation systems. Also, these results indicate that the homogeneous scale of these systems is about 8 Å. In most cases, using a local region radius of 10 Å is a safe choice for 3D-IPSp to reproduce PME results for homogeneous molecular systems.

E. Water interfaces

For heterogeneous systems, the 3D-IPSn/DFFT or 3D-IPSp/DFFT method must be used to accurately calculate long-range interactions. We have demonstrated that for the homogeneous systems 3D-IPSn/DFFT and 3D-IPSp/DFFT produce very similar results (Tables III–V). To further illustrate that the two methods are equally accurate in describing heterogeneous systems, we applied them to a water interface system. A water interface system was created by enlarging the PBC box length of above bulk water system along the z-axis, so that a gas phase was produced above and below the water liquid. There were 2180 TIP3P water molecules in the

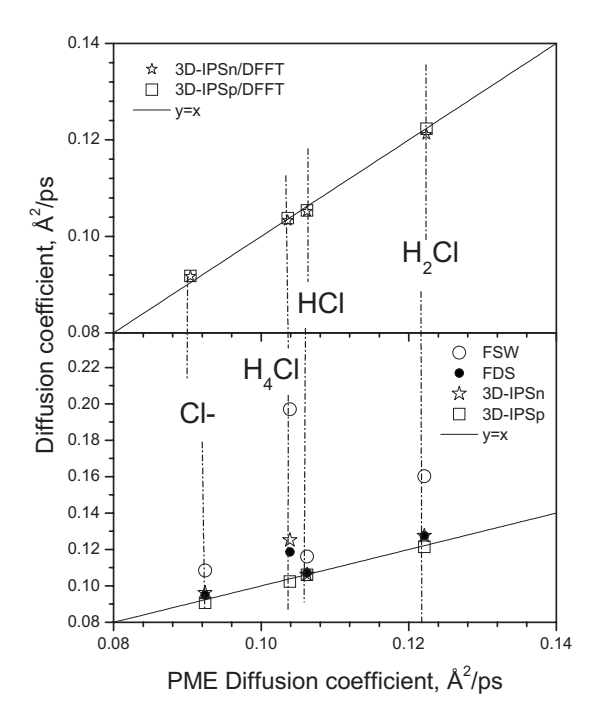


FIG. 5. Diffusion coefficients of the model systems as compared to the PME results. Lower panel shows FSW, FDS, 3D-IPSn, and 3D-IPSp against PME+3D-IPS. Upper panel shows 3D-IPSn/DFFT and 3D-IPSp/DFFT against PME+3D-IPS/DFFT.

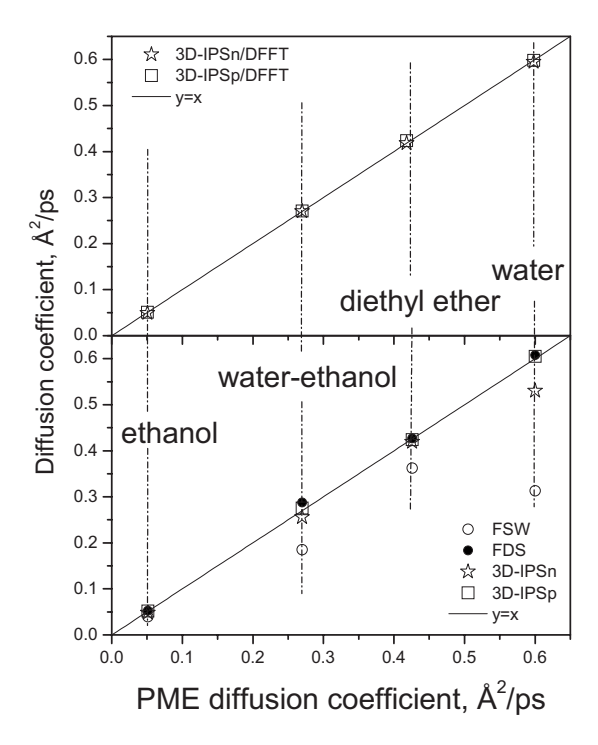


FIG. 6. Diffusion coefficients of the solvent systems as compared to the PME results. Lower panel shows FSW, FDS, 3D-IPSn, and 3D-IPSp against PME+3D-IPS. Upper panel shows 3D-IPSn/DFFT and 3D-IPSp/DFFT against PME+3D-IPS/DFFT.

 $40\times40\times80~\text{Å}^3$ orthorhombic periodic boundary box. This is a typical heterogeneous system involving phase equilibrium. MD simulations of 2 ns at constant temperature (300 K), constant volume ($40\times40\times80~\text{Å}^3$), were performed with both 3D-IPSn/DFFT and 3D-IPSp/DFFT methods.

TABLE VI. Properties of the water interfacial system simulated with 3D-IPSn/DFFT and 3D-IPSp/DFFT.

Properties	3D-IPSn/DFFT	3D-IPSp/DFFT
Potential energy, kcal/mol	$-20\ 233.8 \pm 1.1$	$-20\ 234.2 \pm 1.1$
Energy fluctuation, kcal/mol	68.86 ± 0.51	68.98 ± 0.53
Surface tension, dyn/cm	56.05 ± 0.73	56.51 ± 0.70

Table VI lists the properties from both simulations. The surface tension calculation has been described previously. See As can be seen from Table VI, both simulations produced statistically identical results. Figure 7 shows the electrostatic potentials crossing the water membrane from the two simulations. The difference between the two results is well within the statistical error. Therefore, 3D-IPSp/DFFT is an equally accurate method as the 3D-IPSn/DFFT method for both homogenous and heterogeneous systems.

V. CONCLUSIONS

This work derived the polar 3D-IPS electrostatic potential (3D-IPSp) for polar systems. Through model systems of various polarities, it is demonstrated that the polar electrostatic 3D-IPS potential is accurate for all model systems, while the original electrostatic 3D-IPS potential is limited to monopole and weak polar systems. For the convenience of application, polynomial functions with rationalized coefficients, Eqs. (15), (17), and (18), are proposed to describe 3D-IPS potentials of electrostatic energy and Lennard-Jones dispersion and repulsion energies.

TABLE V. Simulation properties of the model systems at various cutoff distances.

	Properties		3D-	3D-IPSp/DFFT			
Systems		$R_c = 6$ Å	$R_c = 8 \text{ Å}$	$R_c = 10 \text{ Å}$	$R_c = 12 \text{ Å}$	$R_c = 80 \text{ Å}$	PME+3D-IPS
Cl ⁻	Epot, kcal/mol	-1163.2	1284.2	4697.9	8883.5	602 725.3	-3083.1
	D, $Å^2/ps$	0.087	0.094	0.091	0.092	0.091	0.092
	$\delta g_{ ext{Cl-Cl}}$	0.004	0.003	0.002	0.002	0.002	0
HC1	Epot, kcal/mol	-213.2	-104.5	-96.0	-87.8	-78.5	-89.1
	D, $Å^2/ps$	0.101	0.106	0.106	0.105	0.103	0.105
	$\delta g_{ ext{Cl-Cl}}$	0.003	0.002	0.001	0.001	0.001	0
H ₂ Cl	Epot, kcal/mol	1257.4	1401.8	1391.5	1401.1	1407.2	1395.0
-	D, $Å^2/ps$	0.113	0.125	0.122	0.121	0.123	0.124
	$\delta g_{ ext{Cl-Cl}}$	0.006	0.002	0.002	0.002	0.001	0
H ₄ Cl	Epot, kcal/mol	1480.6	1803.9	1743.1	1759.1	1759.1	1744.9
•	D, $Å^2/ps$	0.085	0.110	0.102	0.103	0.102	0.103
	$\delta g_{ ext{Cl-Cl}}$	0.016	0.006	0.002	0.002	0.002	0
Water	Epot, kcal/mol	-20655.4	-20590.2	-20586.0	-20586.6	-20580.8	-20596.2
	D, $Å^2/ps$	0.596	0.607	0.605	0.605	0.604	0.604
	$\delta g_{\mathrm{O-O}}$	0.009	0.002	0.001	0.001	0.001	0
Ethanol	Epot, kcal/mol	-7935.4	-7829.8	-7794.3	-7791.2	-7782.7	-7796.2
	D, $Å^2/ps$	0.063	0.056	0.052	0.051	0.052	0.051
	$\delta g_{\mathrm{O-O}}$	0.042	0.012	0.003	0.004	0.003	0
Mixture	Epot, kcal/mol	-13387.8	$-13\ 308.4$	-13281.4	-13270.3	-13259.3	-13276.3
	D, $Å^2/ps$	0.294	0.280	0.276	0.272	0.271	0.269
	$\delta g_{\Omega=\Omega}$	0.025	0.013	0.006	0.004	0.003	0
Diethyl ether	Epot, kcal/mol	-1855.6	-1781.1	-1747.9	-1743.4	-1729.6	-1737.6
,	D, $Å^2/ps$	0.461	0.423	0.424	0.426	0.421	0.422
	$\delta g_{\mathrm{O-O}}$	0.051	0.016	0.006	0.005	0.004	0

024107-13

FIG. 7. The electrostatic potential profiles cross the water interface system calculated with 3D-IPSn/DFFT and 3D-IPSp/DFFT.

For homogeneous systems, it is demonstrated through model systems and solvent systems that the 3D-IPSp potential with a local region radius of as small as 10 Å produces almost identical structural, dynamic, and thermodynamic properties as the PME method. The computational cost is comparable to that of other cutoff-based methods.¹⁴

When implemented to the 3D-IPS/DFFT method, the 3D-IPSp potential produces very similar results as the 3D-IPSn potential for both homogeneous and heterogeneous systems. Due to the use of DFFT, the computational cost is comparable to that of PME. ^{15,16}

Because the polar electrostatic 3D-IPS potential can describe nonpolar systems equally well, it will be used as the default in the future for the calculation of electrostatic interactions. If not otherwise stated, the electrostatic 3D-IPS potential will by default mean the polar electrostatic 3D-IPS potential or 3D-IPSp.

ACKNOWLEDGMENTS

We thank Richard Pastor and Richard Venable for many fruitful discussions. X.W. thanks Michael J. Foycik, Jr. for his help with the manuscript.

- ¹P. J. Steinbach and B. R. Brooks, J. Comput. Chem. 15, 667 (1994).
- ²M. Bergdorf, C. Peter, and P. H. Hunenberger, J. Chem. Phys. 119, 9129 (2003).
- N. A. Baker, V. Helms, and J. A. McCammon, Proteins 36, 447 (1999).
 J. A. Barker and R. O. Watts, Mol. Phys. 26, 789 (1973).
- ⁵J. D. Weeks, Annu. Rev. Phys. Chem. **53**, 533 (2002).
- ⁶P. H. Hunenberger and W. F. van Gunsteren, J. Chem. Phys. **108**, 6117 (1998); N. A. Denesyuk and J. D. Weeks, *ibid.* **128**, 124109 (2008); J. M. Rodgers and J. D. Weeks, Proc. Natl. Acad. Sci. U.S.A. **105**, 19136 (2008)
- ⁷ D. Wolf, P. Keblinski, S. R. Phillpot, and J. Eggebrecht, J. Chem. Phys. 110, 8254 (1999).
- ⁸F. N. Mendoza, J. Lopez-Lemus, G. A. Chapela, and J. Alejandre, J. Chem. Phys. **129**, 024706 (2008).
- ⁹C. J. Fennell and J. D. Gezelter, J. Chem. Phys. **124**, 234104 (2006).
- ¹⁰ S. Izvekov, J. M. J. Swanson, and G. A. Voth, J. Phys. Chem. B **112**, 4711 (2008).
- ¹¹P. P. Ewald, Ann. Phys. **64**, 253 (1921).
- ¹²U. Essmann, L. Perera, M. L. Berkowitz, T. Darden, H. Lee, and L. G. Pedersen, J. Chem. Phys. **103**, 8577 (1995).
- ¹³ W. Weber, P. H. Hunenberger, and J. A. McCammon, J. Phys. Chem. B 104, 3668 (2000).
- ¹⁴X. Wu and B. R. Brooks, J. Chem. Phys. 122, 044107 (2005).
- ¹⁵ X. Wu and B. R. Brooks, J. Chem. Phys. 129, 154115 (2008).
- ¹⁶ R. M. Venable, L. E. Chen, and R. W. Pastor, J. Phys. Chem. B 113, 5855 (2009).
- ¹⁷ A. J. Stone, *The Theory of Intermolecular Forces* (Clarendon, Oxford, 1996).
- ¹⁸ A. D. MacKerell, Jr., D. Bashford, M. Bellott, R. L. Dunbrack, Jr., J. D. Evanseck, M. J. Field, S. Fisher, J. Gao, H. Guo, S. Ha, D. Joseph-McCarthy, L. Kuchnir, K. Kuczera, F. T. K. Lau, C. Mattos, S. Michnick, T. Ngo, D. T. Nguyen, B. Prodhom, W. E. Reiher III, B. Roux, M. Schlenkrich, J. C. Smith, R. Stote, J. Straub, M. Watanabe, J. Wiorkiewicz-Kuczera, D. Yin, and M. Karplus, J. Phys. Chem. B 102, 3586 (1998).
- ¹⁹ S. E. Feller, R. W. Pastor, A. Rojnuckarin, S. Bogusz, and B. R. Brooks, J. Phys. Chem. **100**, 17011 (1996).
- ²⁰B. R. Brooks, R. E. Bruccoleri, B. D. Olafson, D. J. States, S. Swaminathan, B. Jaun, and M. Karplus, J. Comput. Chem. 4, 187 (1983); B. R. Brooks, C. L. Brooks III, A. D. Mackerell, Jr., L. Nilsson, R. J. Petrella, B. Roux, Y. Won, G. Archontis, C. Bartels, S. Boresch, A. Caflisch, L. Caves, Q. Cui, A. R. Dinner, M. Feig, S. Fischer, J. Gao, M. Hodoscek, W. Im, K. Kuczera, T. Lazaridis, J. Ma, V. Ovchinnikov, E. Paci, R. W. Pastor, C. B. Post, J. Z. Pu, M. Schaefer, B. Tidor, R. M. Venable, H. L. Woodcock, X. Wu, W. Yang, D. M. York, and M. Karplus, *ibid.* 30, 1545 (2000)
- ²¹J. P. Ryckaert, G. Ciccotti, and H. J. C. Berendsen, J. Comput. Phys. 23, 327 (1977).
- ²² J. B. Klauda, X. Wu, R. W. Pastor, and B. R. Brooks, J. Phys. Chem. B 111, 4393 (2007).
- ²³ T. Darden, L. Perera, L. Li, and L. Pedersen, Structure (London) 7, R55 (1999).